Journal of Building Engineering 122 (2026) 115767

Contents lists available at ScienceDirect

Journal of Building Engineering

journal homepage: www.elsevier.com/locate/jobe

Full length article

Influence of thermally activated artificial concrete fines composition on concrete long-term behavior

Jan P. Höffgen *, Marius Schmitt, Frank Dehn

Karlsruhe Institute of Technology (KIT), Institute for Concrete Structures and Building Materials (IMB), Gotthard-Franz-Str. 3, Karlsruhe, 76131, Germany

ARTICLE INFO

Keywords:
Concrete
Cement
Mineral waste
Recycling
Thermal activation
Supplementary cementitious material

ABSTRACT

Thermal activation of concrete fines is a promising method for the simultaneous reduction of CO_2 emissions and mineral waste. Hydrated cement paste, a major component of these recycled materials, can be used as a reactive supplementary cementitious material after dehydration at elevated temperatures and grinding. This affects concrete strength, especially when fines contain a higher proportion of aggregates. While strength loss can be mitigated by adjusting the water-binder ratio, the combined effect on other mechanical properties and durability remains unclear. This study utilizes seven different artificial concrete fines with varying binder compositions, aggregate contents, and aggregate mineralogies to produce concrete with varying compressive strengths. These concretes are then assessed for their flexural strength, elastic modulus, shrinkage, water absorption, chloride diffusion, carbonation, and freeze-thaw-resistance. Results highlight that with increasing compressive strength, mechanical properties and durability also improve. However, while strength development and the elastic modulus are similar to the reference concrete, the substitution of Portland cement through activated fines increases shrinkage as well as carbonation and chloride ingress, especially for fines with a high amount of reactive SiO_2.

1. Introduction

Thermal activation of concrete fines is a promising process for mineral construction and demolition waste recycling, as well as reducing the carbon footprint of cement production [1–9]. The activation process relies on the dehydration of hydrated cement paste (HCP) within these fines. With increasing temperature, different cement hydration products gradually release chemically bound water. Most prominently, calcium hydroxide disintegrates to free lime in the temperature range of 400 °C to 550 °C, and calcium silicate hydrates decompose between 110 °C and 500 °C to form reactive $\alpha'_H C_2S$ and $\alpha'_L C_2S$ [10–23]. Upon re-wetting, the activated paste rapidly rehydrates, recreating the original cement phases [10,12,13,16,17,19,24–27]. Because both the hydrated and the dehydrated paste remain porous, the rehydrated product primarily occupies the existing pore network, resulting in limited inter-particle bonding and reduced strength [17,18,25,28–30].

When used as a supplementary cementitious material (SCM), thermally activated cement paste can replace up to 25 wt% – 40 wt% of ordinary Portland cement (OPC) without significantly compromising compressive strength [14,29,31–36]. The behavior stems from the high water consumption of the activated particles, which lowers the free water available for OPC hydration and thus densifies the matrix [29,34,37]. For higher substitution rates, total porosity increases alongside decreasing compressive strength [14,18]. Similarly, incomplete dehydration at activation temperatures below 400 °C leads to increased porosity [18,37].

* Corresponding author.
E-mail address: jan.hoeffgen@kit.edu (J.P. Höffgen).

https://doi.org/10.1016/j.jobe.2026.115767
Received 7 October 2025; Received in revised form 12 December 2025; Accepted 1 March 2026
Available online 4 March 2026

While compressive strength is the central material property, durability and deformation behavior are major factors in concrete design. Besides affecting compressive strength, the substitution of Portland cement through activated concrete fines as supplementary cementitious materials (SCMs) also changes material resistance to corrosion (e.g., carbonation, chloride ingress, or freeze-thaw action) as well as elastic or shrinkage deformations.

Substituting OPC with activated fines generally reduces the elastic modulus due to the lower density of the fines [24], but the effect persists even at modest replacement levels [38,39]. Shrinkage deformations follow a similar trend with increased deformations [38,40]. Low-level substitution can be offset by the densification effect, whereas high-temperature activation or lower water-cement ratios in the precursor material increase particle stiffness and mitigate shrinkage [38,40–42]. Besides, drying shrinkage is affected by the amount of evaporable water, and increases when additional mixing water is used to compensate for the high water demand of activated cement paste [40,41].

Capillary absorption follows the same influencing factors as paste porosity. Higher Portland cement substitution through activated cement paste results in increased absorption, especially when additional mixing water is used for adjusting fresh concrete workability [40]. At a fixed water-binder ratio, the reduction of free water outside of activated cement paste particles lessens capillary absorption [31,40,43]. Compared to ground HCP, thermal activation at up to 1000 °C reduces absorption [33,36,41,42,44]. Water absorption plays an important role in freeze-thaw damage evolution. At similar strength, mortar and concrete containing thermally activated concrete fines exhibit a similar freeze-thaw-resistance as Portland cement reference mixes [45,46]. The diffusion of Cl^- and CO_2 is affected by paste porosity and the binding capacity of hydration products. Subsequently, the aforementioned influences on porosity impact the resistance to carbonation and chloride ingress [28,29,31,43,47,48].

Assessing mechanical and durability properties after partial substitution of Portland cement with thermally activated concrete fines remains challenging, primarily because the substitution also affects compressive strength. This interdependence obscures the isolated effects of the fines themselves. For pure OPC-based HCP, such strength variations may be limited. However, concrete fines sourced from recycling plants contain aggregates of varying amounts and mineralogical compositions, and may incorporate hydration products from alternative binders (e.g., slag, pozzolans). These components alter both reactivity and mechanical performance in ways that are not yet predictable. Although the aggregate fraction of concrete fines is widely recognized as essentially inert and therefore detrimental when used as SCM, the contribution of alternative binder residues remains much less clear [24,43,49–54]. The existing literature regularly uses concrete with fixed water-binder ratios, or increased water contents to compensate for insufficient workability, and therefore does not provide a consistent framework for distinguishing the effects of composition from those of strength change.

In practice, when designing concrete to meet a defined compressive strength, a possible negative impact of SCMs on the latter is usually compensated for by a reduction of the water-binder ratio. Although the procedure can restore compressive strength, it does not uniformly affect other mechanical or durability properties. However, codes and standardized structural design implicitly assume that concretes with the same compressive strength will exhibit comparable deformation behavior and reinforcement corrosion resistance. This assumption has never been validated for systems that incorporate thermally activated concrete fines. No previous study has systematically examined whether restoring compressive strength also recovers mechanical and durability responses altered by the heterogeneous composition of the fines.

2. Experimental program

The experimental program is structured to address this unresolved question directly. The central objective is to determine whether compensating for the strength reduction caused by activated concrete fines also neutralizes their influence on the deformation characteristics and the durability performance. For this means, artificial fines with controlled and varying amounts of inert aggregate and alternative binder residues, and thus varying compressive strength contribution, are employed. By holding compressive strength constant across mixtures, the study isolates the macroscopic effects arising solely from fines composition. This approach provides the first systematic evaluation of whether established empirical relationships linking mechanical and durability behavior to compressive strength remain valid in concretes containing thermally activated fines.

2.1. Materials

Base materials for the experimental procedures were a commercial Portland cement CEM I 42.5 R (“CEM I”), ground granulated blast-furnace slag (“S”) and black coal fly ash (“FA”) as binders, as well as siliceous river sand (0/2 mm, “RS”) and gravel (2/8 mm, “RG”), limestone sand (0/4 mm, “LS”) and greywacke (0/4 mm, “GW”) as aggregates.

Seven different artificial fines were used as representative concrete fines to set up three groups of three (see Table 1). One group altered the binder composition, where, starting with CEM I-paste (“CEM”), 30 wt% of the binder were substituted for fly ash (“FA0”) or slag (“S0”). The second group varied binder content, where RS replaced 50 v% (“RS50”), and 25 v% (“RS75”) of the CEM I-paste (“CEM”). Finally, the third group switched the river sand in RS50 for LS and GW with different aggregate compositions (“LS50” and “GW50”). The artificial fines chosen for the present study resemble possible compositions found in literature. [55] contains a detailed mix design, as well as characterization of the artificial fines performance.

For all artificial fines, three prisms ($(40 \times 40 \times 160)\,mm^3$) were cast, and cured alongside the bulk materials. Bulk materials were stored in sealed buckets with excess water, and demolded after at least nine months to exclude the influence of temporal effects from the subsequent analyses. Samples were dried at 105 °C before grinding in an industrial mill. The temperature of the grinding tube was monitored to not exceed 100 °C.

Table 1
Composition of artificial fines with water-binder ratio $w/b = 0.5$. v_p: paste volume; Agg.: aggregates; FA: fly ash; S: blast-furnace slag; RS: river sand; LS: limestone sand; GW: greywacke.

	Binder	v_p[v%]	Agg.
CEM	100 wt% CEM I	100	–
FA0	70 wt% CEM I + 30 wt% FA	100	–
S0	70 wt% CEM I + 30 wt% S	100	–
RS75	100 wt% CEM I	75	RS
RS50		50	RS
LS50		50	LS
GW50		50	GW

Table 2
Mix design of the reference series CEM I-2.

	Density g/cm³	Share kg/m³
River gravel 2/8 mm	2.56	1024
River sand 0/2 mm	2.63	526
CEM I 42.5 R	3.13	488
Water	1.00	244

Afterwards, artificial fines were thermally activated in a static furnace. The target temperature of 600 °C (suffix "−600") was held constant for 6 h. The heating ramp was controlled (5 K/min), while cooling was limited to the passive cooling of the furnace. When reaching 100 °C, samples were stored in sealed containers with a drying agent to prevent moisture ingress. Two types of artificial fines (CEM and RS50) were additionally activated at 400 °C ("−400"), and also used in their ground variant ("−100"). [56] details the thermal activation procedure.

2.2. Experimental procedures

The raw materials were analyzed for their chemical composition through WDXRF measurements (EN 196-2:2013), and their mineralogical composition through XRD. Artificial fines and CEM I were characterized for their chemical composition (wet-chemical analysis and carbon-sulfur analysis, EN 196-2:2013), particle size distribution (laser diffraction), and particle density (pycnometer). Nitrogen absorption/desorption was used to determine both the specific surface areas (BET method) and porosity (BJH method).

Concrete was designed with an aggregate content of 60 v%, split into 20 v% RS (0/2 mm) and 40 v% RG (2/8 mm), which was held constant for all concrete mixes. Sieve analyses yielded $d_{10} \approx 0.12$ mm, $d_{50} \approx 0.34$ mm, and $d_{90} \approx 0.88$ mm for RS, as well as $d_{10} \approx 2.8$ mm, $d_{50} \approx 4.9$ mm, and $d_{90} \approx 7.0$ mm for RG. Limiting the maximum grain size to 8 mm enabled the use of smaller specimen sizes. This subsequently reduced raw material consumption. While this came at the cost of potentially increased scatter, following the size-effect law, it reduced time-intensive thermal activation and allowed for the testing of all material properties from a single batch of concrete per mix. For each binder, two different water-binder ratios (w/b) were adopted: Series 1 used $w/b = 0.5$, without taking artificial fines reactivity into account. Series 2 applied the equivalent concrete performance concept defined in EN 206:2021 and CEN/TR 16639:2014, where $w/c_{eq} = 0.5$ replaces w/b (Eq. (1)).

$$\frac{w}{c_{eq}} = \frac{w}{c + k \cdot a} \qquad \text{with } a\text{: SCM-content} \tag{1}$$

The k-value addresses the performance of individual SCMs compared to Portland cement. For $k = 1.0$, the equivalent water-cement ratio equals the water binder ratio, while an alteration of w/b compensates for the effect of Portland cement substitution on concrete performance through SCMs. k-values for individual processed artificial fines were determined in a previous study on compressive strength and subsequently applied in the present work [55]. For each SCM, the water-binder ratio was adjusted to reach the target $w/c_{eq} \approx 0.5$.

Similarly, two reference series without CEM I substitution were defined with $w/b = w/c_{eq} = 0.6$ ("−1") and $w/b = w/c_{eq} = 0.5$ ("−2"). Mixes of CEM I-1 and CEM I-2 were produced twice to enable double determinations of select material properties. For the assessment of activated artificial fines as SCM, a substitution rate of 30 wt% of CEM I was selected. Additionally, CEM-600 and RS50-600 were also used to replace 10 wt% and 50 wt% of CEM I. The mix design for the reference series CEM I-2 is listed in Table 2. Table A.5 in the appendix gives an overview of the different series.

During concrete mixing, workability was adjusted through the addition of superplasticizer. Target consistency was a spread of 17 cm – 19 cm determined by the flow table test in EN 1015-3:2007. After being placed in steel molds, samples were kept humid at 20 °C until demolding at 1 d. Afterwards, specimens were cured depending on the conditioning plan for each concrete property. Unless otherwise stated, all procedures were performed at 20 °C. The subsequent experimental analyses required compromises to enable the determination of various concrete performance indicators from a single batch. The selection of specimen sizes followed the requirement in EN 12390-1:2011 of a minimum size of 28 mm for a maximum aggregate diameter of 8 mm. Fig. A.14 gives an overview of the experimental setups for concrete testing.

Strength development. Strength testing followed the provisions in European standard EN 196-1:2016 and used six prisms ($(40 \times 40 \times 160)\,mm^3$), which were cured underwater. Despite being a test procedure for cement mortar, this choice enabled the determination of two strength parameters on a single specimen. Flexural tests were performed on three prisms at concrete ages of 2 d and 28 d. Compressive tests used three prism halves immediately after flexural tests. The remaining halves were tested at 56 d and 98 d.

Dynamic modulus of elasticity. For the determination of the dynamic modulus of elasticity, three prisms ($(40 \times 40 \times 160)\,mm^3$) were moist cured at 100 % r. h. until the age of 7 d and subsequently stored at 65 % r. h. until the determination of the dynamic moduli through ultrasonic pulse measurements at the concrete age of 28 d.

The dynamic modulus of elasticity E_c was derived from ultrasonic pulse velocity v_u, specimen density ρ_p, and Poisson's ratio ν using Eq. (2). Afterwards, flexural and compressive strength were determined on the same prisms following the provisions in EN 196-1:2016.

$$E_c = v_u^2 \cdot \rho_p \cdot \frac{(1+\nu)(1-2\cdot\nu)}{1-\nu} \tag{2}$$

Shrinkage. Three prisms ($(40 \times 40 \times 160)\,mm^3$) for shrinkage were produced with cast-in pins and stored alongside specimens for dynamic modulus measurements. Deformation and mass loss were determined at a concrete age of 1 d, 7 d (t_0), 14 d, 21 d, 35 d, 63 d, and 98 d, followed by strength tests after the last deformation testing according to EN 196-1:2016.

Shrinkage deformations ε_{cs} were obtained from normalizing the measured absolute length change to the specimen length after demolding.

Chloride diffusion. From each concrete mix, one cylinder ($d = 100\,mm, h = 280\,mm$) was produced and stored underwater after demolding. Water curing was interrupted for cutting the cylinder into 5 slices ($h \approx 45\,mm$) and covering the lateral surfaces of all 5 specimens and one flat surface of three specimens with epoxy resin. At the age of 28 d, these three specimens were taken from the water bath and submerged in a saturated $Ca(OH)_2$-solution for 24 h before being placed in a 16.5 wt%-NaCl-solution for 35 d. While this conditioning follows European standard EN 12390-11:2015, a simplified representative chloride penetration depth was determined using silver nitrate as an indicator on cracked specimens, similar to the rapid chloride migration test in EN 12390-18:2021. The average penetration depth d_c was obtained as the average of nine data points from each cracked surface per specimen.

Capillary absorption. Capillary absorption tests were performed on the two remaining cylindrical specimens, with only the lateral surfaces coated in epoxy resin. After water curing until the age of 28 d, the specimens were stored at 65 % r.h. for at least 6 months, until they reached a constant mass. To determine the capillary absorption coefficient $WA_{24\,h}$, the mass change of each specimen after partial submersion of the bottom 5 mm for 24 h was measured and normalized to the surface area.

Carbonation. The determination of the accelerated carbonation coefficient K_{AC} followed the procedure in EN 12390-12:2020. Three prisms ($(40\times40\times160)\,mm^3$) were stored underwater until the age of 28 d with a subsequent dry storage at 65 % r.h. for 14 d. Afterwards, specimens were exposed to 3 v% CO_2 at 57 % r.h. for another 70 d, with intermediate testing ages after 7 d and 28 d exposure. For each determination, a fresh surface from each prism was produced by splitting. After applying a phenolphthalein indicator, the mean carbonation depth $d_{k,t}$ was determined from three measuring points per edge per specimen. K_{AC} was then calculated as the slope of a straight line fitted to the mean carbonation depth over the square root of the duration of the exposure t, using the least squares method on Eq. (3).

$$d_k = K_{AC} \cdot \sqrt{t} \tag{3}$$

Freeze-thaw-cycles. Freeze-thaw tests were based on the cube test in the technical specification CEN/TS 12390-9:2017. Two cubes (100 mm) from mixtures with $w/c_{eq} = 0.5$ were stored underwater until the age of 7 d with a subsequent dry storage at 65 % r.h. for 21 d. Afterwards, both specimens were submerged in a container filled with demineralized water and placed in the freeze-thaw chamber. The first freeze-thaw cycle started after another 24 h, where specimens were left to absorb water. Freezing to −15 °C followed the ramp defined in CEN/TS 12390-9:2017, and for thawing, the chamber was filled with warm water. When the temperature in the specimen container had reached 20 °C, fragments were brushed off and the mass of all fragments was determined through oven-drying. Measurements were taken after 7, 14, and 28 freeze-thaw cycles (FTC), with some test extensions to 56 FTC.

Porosity. For the quantification of porosity through mercury-intrusion, concretes were mirrored through additional paste specimens with the same ratio of CEM I to SCM to water, but without aggregates. Immediately after mixing, samples were left in sealed flasks until demolding and crushing to a particle size of 2 mm – 4 mm at the age of 28 d. Following a solvent exchange through isopropyl, samples were dried at 60 °C before testing.

3. Results and discussion

3.1. Characterization of binders

The physical and chemical characterization of CEM I and the processed artificial fines highlights differences between both groups, as well as between artificial fines of different compositions and activation temperatures (see Tables 3 and 4). For reference, Figs. A.15 and A.16 illustrate the mineralogical composition of the raw materials.

Table 3
Results of the physical analysis of CEM I and activated artificial fines. ρ_p: Particle density (pycnometer), S_{BET}: Specific surface area (BET-Method), p_{BJH}: Pore volume (desorption, BJH-Method) d_{10}, d_{50}, d_{90}: Particle size at 10 v%, 50 v%, and 90 v% cumulatively passing (laser diffraction)

	ρ_p kg/dm^3	S_{BET} m^2/g	p_{BJH} cm^3/kg	d_{10} µm	d_{50} µm	d_{90} µm
CEM I	3.13	1.39	7.08	1.7	12.1	32.9
CEM-100	2.35	18.42	102.15	2.0	14.8	51.8
CEM-400	2.45	14.08	90.98	2.1	16.2	60.8
CEM-600	2.69	14.55	94.56	1.8	14.0	51.1
FA0-600	2.72	11.09	66.35	2.3	23.6	76.7
S0-600	2.77	10.48	63.88	2.1	21.5	76.0
RS75-600	2.77	7.53	47.16	1.7	13.5	51.5
RS50-100	2.54	6.51	36.56	1.9	15.3	50.8
RS50-400	2.59	5.45	33.72	1.9	14.7	49.3
RS50-600	2.59	5.41	33.08	1.9	14.5	49.7
LS50-600	2.73	6.13	35.74	1.6	12.6	74.7
GW50-600	2.72	7.98	42.08	1.7	12.4	51.5

Table 4
Results of the wet-chemical analysis of CEM I and activated artificial fines. Carbon (C), total and reactive (r-)CaO, and total and reactive (r-)SiO_2, all according to EN 196-2:2013, and free f-CaO according to EN 451-1:2017.

	C wt%	CaO wt%	f-CaO wt%	r-CaO wt%	SiO_2 wt%	r-SiO_2 wt%
CEM I	0.5	61.7	0.8	57.7	20.4	19.5
CEM-100	1.0	51.4	12.8	45.4	16.9	16.2
CEM-400	1.2	54.0	11.7	46.9	18.0	17.2
CEM-600	1.3	58.1	7.1	50.7	19.2	18.6
FA0-600	0.9	43.0	0.1	38.0	29.0	26.4
S0-600	0.8	50.1	0.8	45.3	28.0	24.1
RS75-600	1.0	40.8	1.8	35.9	39.6	18.1
RS50-100	1.0	21.1	3.5	17.3	53.3	7.8
RS50-400	1.1	21.8	2.9	17.7	59.1	12.5
RS50-600	1.1	22.0	0.0	18.0	60.1	14.1
LS50-600	7.6	49.4	0.1	13.4	12.0	9.2
GW50-600	0.6	18.2	0.1	16.8	56.1	22.9

Particle density ρ_p, specific surface area S_{BET}, and pore volume p_{BJH} are interdependent: A high density coincides with a low porosity and low specific surface area, exemplified through CEM I. Dried, hydrated cement paste, CEM-100, on the other hand, exhibits the lowest density and highest porosity and specific surface area among the artificial fines. The thermal activation has a densifying effect on the microstructure (compare [18]). Similarly, the effect of hydration products from slag or fly ash yields a denser paste (compare [53,54]). The presence of aggregates results in a reduced paste volume and subsequently increased particle density and reduced specific surface area and porosity (Table 3).

The chemical composition of the processed artificial fines is defined through the composition of the raw materials (see Table A.6). Yet, the wet-chemical analysis allows for a more detailed analysis. For CEM I, the total amount of CaO and SiO_2 matches the results from WDXRF. Table 4 shows that most of these are in a reactive form. When CEM I chemically binds water, the resulting artificial fines CEM-100 have a relatively lower amount of both CaO and SiO_2. During hydration, cement clinker forms calcium hydroxide, which is subsumed in free CaO, and other hydrates, whose calcium content comprises reactive CaO. Due to the loss of chemically bound water during thermal activation, (reactive) CaO and (reactive) SiO_2 increase for CEM-400 and CEM-600. Free CaO decreases, which exists as $Ca(OH)_2$ in CEM-100 and converts to CaO with increasing temperature. However, the offset indicates the formation of additional phases.

Compared to CEM-600, S0-600, and FA0-600, where CEM I was partially replaced by slag or fly ash during artificial fines production, exhibit a significantly higher amount of (reactive) SiO_2, in favor of a reduced amount of reactive and free CaO.

Artificial fines containing quartzitic river sand (RS) as aggregates (RS50 and RS75) have a reduced amount of reactive CaO and SiO_2 compared to CEM. However, the present results suggest an interaction between free CaO and (inert) SiO_2 during thermal activation. Free CaO in RS50-100 is completely consumed, while the amount of reactive SiO_2 almost doubles. RS75-600 shows similar results, which cannot solely be explained when considering these artificial fines as a blend of CEM and inert river sand. The analysis of artificial fines LS50-600 and GW50-600. LS50-600 with calcitic aggregates comprises a low amount of reactive components. GW50-600, on the other hand, contains greywacke with amorphous SiO_2, which increases the amount of reactive SiO_2 in the activated artificial fines.

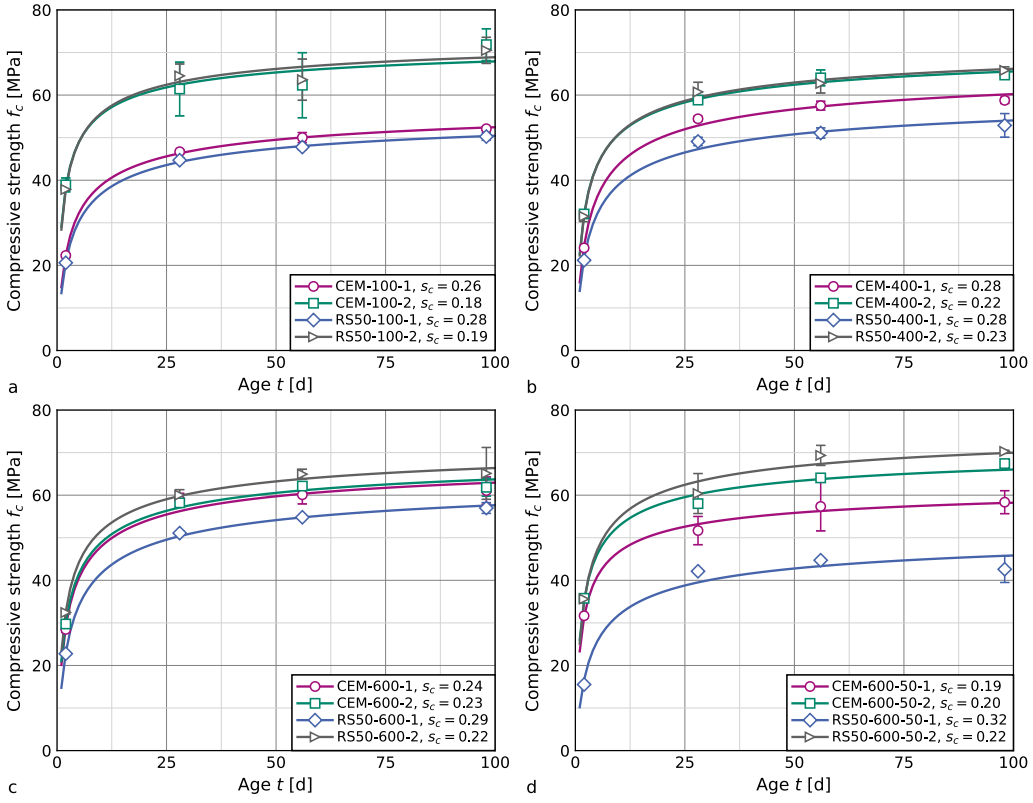

Fig. 1. Temporal compressive strength development of select concrete mixtures with artificial fines "CEM" and "RS50" processed at different temperatures and at different substitution rates. Markers and error bars represent mean values and standard deviations from three prism halves. Lines indicate optimized fit curves for strength development according to Eq. (4).

The results in Table 4 also show that all artificial fines contain carbon (C), which can only partially be explained by the raw material composition. This suggests that despite careful handling of artificial fines, natural carbonation, i.e., during milling, could not completely be avoided. The amount of organic carbon (TOC) was 0.0 wt% for all materials.

3.2. Compressive strength development

Fig. 1 illustrates selected results for concrete mixes containing processed artificial fines "CEM" and "RS50", and data processing of compressive strength tests.

For all concrete mixes, compressive strength results from series 2 are close to each other. Independent of concrete age at testing, concrete containing CEM-100 or RS50-100 exhibits similar compressive strength for each series individually. At all ages, compressive strength for series 2, where the water-binder ratio was reduced based on individual k-values, exceeds results from series 1. Compressive strength of series 1 for both types of artificial fines increases with higher processing temperature, more so for CEM than for RS50, where CEM-600 (with $k = 1.0$) reaches the same strength for both series. This also underlines the overall good reproducibility of the results. Increasing the substitution rate from 30 wt% to 50 wt% results in decreasing concrete strength, with RS50-600-50-1 exhibiting the lowest overall compressive strength of all investigated concrete mixes. Yet, the results for RS50-600-50-2 show that this compressive strength reduction can be compensated for by lowering the water-binder ratio.

The temporal compressive strength development can be further analyzed through two different approaches. Eq. (4) appropriates the model for compressive strength development in *fib* Model Code 2020 [57] for $t_{ref} = 28$ d. The equation was fitted to the experimental data by the least-squares method for each concrete mix. The fit yielded a stabilized reference strength $f_{cm,ref}$ and a strength development parameter s_c. Fig. 1 contains fit results for Eq. (4) for each individual mix. Alternatively, r (Eq. (5)) directly uses the ratio of compressive strength at 2 d and 28 d. However, while r can be more easily determined, this parameter is more sensitive to scatter.

$$f_c(t) = f_{cm,ref} \cdot \exp\left\{ s_c \cdot \left[1 - \left(\frac{t_{\mathrm{ref}}}{t} \right)^{0.5} \right] \right\} \qquad \text{with } t_{ref} = 28\,\mathrm{d} \tag{4}$$

$$r = \frac{f_{c,2\,\mathrm{d}}}{f_{c,28\,\mathrm{d}}} \tag{5}$$

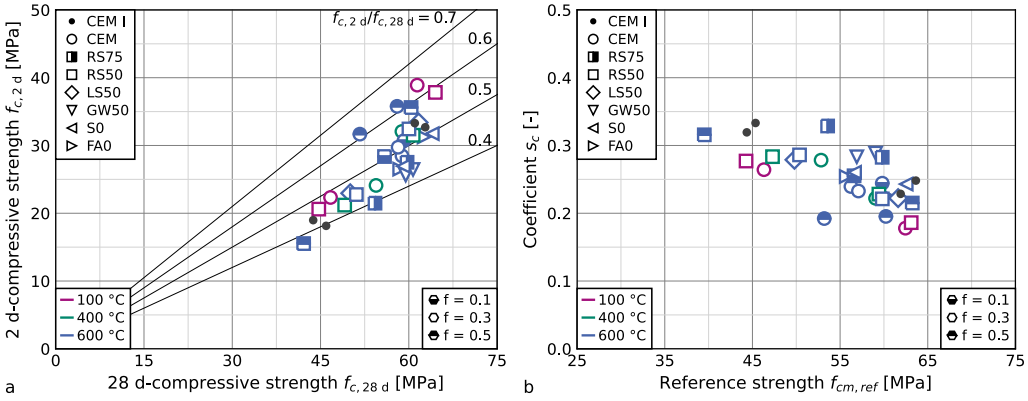

Fig. 2. Temporal compressive strength development of concrete containing processed artificial fines as SCM. Marker shapes indicate different artificial fines, fill styles indicate substitution rates (f), and color indicates processing temperatures.
(a): Compressive strength after 2 d over compressive strength after 28 d. Straight lines indicate strength ratio r (see Eq. (5))
(b): Parameters $f_{cm,ref}$ and s_c as results from fitting Eq. (4) to experimental results after 2 d, 28 d, 56 d and 98 d.

Fig. 2 illustrates the results for both approaches. Increasing $f_{c,28\,d}$ comes with disproportionally increased $f_{c,2\,d}$. Regardless of artificial fines composition (which affects compressive strength differently, as seen by the width of results for compressive strength in general), r ranges from <0.4 for the lowest strength concrete to >0.6 for the highest strength concrete. Similarly, s_c decreases from >0.3 to <0.2.

This behavior is well known. The *fib* Model Code 2020 [57] proposes $s_c = 0.2$ for concrete with CEM I 42.5 R and 35 MPa < f_{ck} < 60 MPa, and $s_c = 0.3$ for $f_{ck} \leq 35$ MPa. Here, f_{ck} denotes the characteristic compressive strength measured on cylinders. For comparison, the present analysis assumes prism compressive strength to exceed characteristic compressive strength by 18 MPa. This simplified offset comprises the difference between characteristic and mean compressive strength (8 MPa) and between cylindrical and cube compressive strength (10 MPa for 35 MPa < f_{ck} < 60 MPa). Therefore, the present results for concrete with varying artificial fines compositions and substitution rates, including the CEM I-reference, agree well with the provisions in *fib* Model Code 2020 [57] for the present compressive strength range.

When assessing the influence of artificial fines composition, most materials exhibit a similar behavior, regardless of binder composition or aggregate composition. Only RS75 and GW50 show a slower strength development, indicated through increased s_c. The latter can be explained by the pozzolanic nature of greywacke [51]. The behavior of RS75 remains inexplicable, as the expected results would lie in the range of RS50 and CEM. The thermal activation of RS50 and CEM at 400 °C or 600 °C results in slower strength development compared to 100 °C. The filler effect is present from the start and does not increase compressive strength at a later age, while rehydration of dehydrated fines is faster than CEM I hydration, but still time-dependent. Consequently, s_c for concrete with processed artificial fines reduces with higher substitution rates.

Despite the good agreement of the experimental data and the empirically fitted empirical approach in Eq. (4), there are some residual deviations. This is exemplified by both series RS50-600-50, where the 28 d-strength of the "−1"-mix exceeds the fitted curve, while the results for the "−2"-series exhibit the contrary behavior. Therefore, for the subsequent assessment of shrinkage and durability, where compressive strength was not directly measured, $f_{cm,ref}$ was used instead of $f_{c,28\,d}$ to reduce the potential impact of scatter.

3.3. Dynamic modulus of elasticity

As the experimental determination of the static modulus of elasticity is a time-consuming process, which could not be integrated into the extensive experimental program, the dynamic modulus of elasticity was measured as an inexpensive substitute. Since the aggregate fraction and content, as well as curing conditions, were held constant for all series, the results derived from ultrasonic pulse measurements allow for the qualitative assessment of the influence of the use of artificial fines as SCM [58,59].

Fig. 3 illustrates results for the dynamic modulus of elasticity and compressive strength at the age of 28 d measured on the same concrete specimens.

Overall, the modulus of elasticity increases with increasing compressive strength, corroborating findings in [39] for varying substitution rates. The results show only small deviations of concrete containing processed artificial fines as SCM from the trend set by the CEM I-references. Only series with thermally activated paste (CEM, S0, and FA0) as well as GW50, which contains an increased amount of reactive silica, exhibit a marginally smaller dynamic modulus of elasticity as compared to other series with similar compressive strength. These findings agree with [38], where reduced ultrasonic pulse velocity was linked to higher particle porosity of dehydrated paste and decreasing cement matrix stiffness.

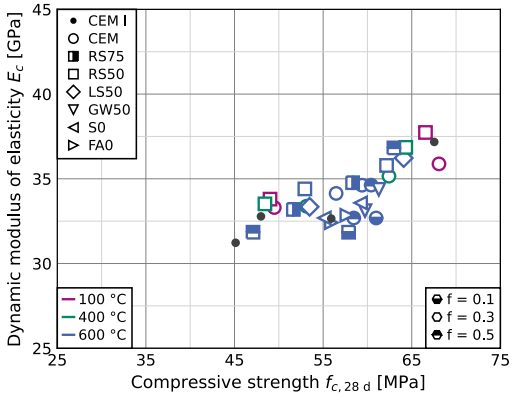

Fig. 3. Dynamic modulus of elasticity and compressive strength at the age of 28 d for different concrete mixes. Marker shapes indicate different artificial fines, fill styles indicate substitution rates (f), and color indicates processing temperatures.

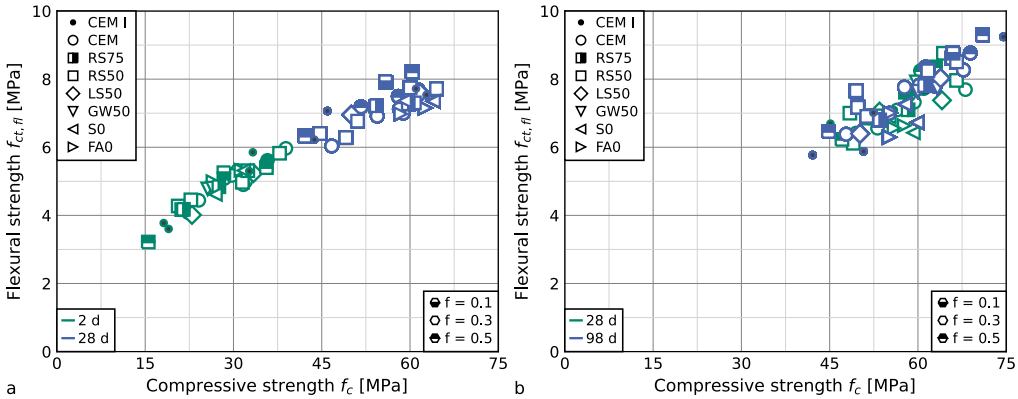

Fig. 4. Flexural and compressive strength at different ages for different concrete mixes. Marker shapes indicate different artificial fines, fill styles indicate substitution rates (f), and color indicates processing temperatures. (a): wet-stored prisms at the ages of 2 d and 28 d, (b): dry-stored prisms at the ages of 28 d and 98 d.

3.4. Flexural strength

The adoption of the test setup from EN 196-1:2016 allows for the determination of flexural and compressive strength on the same concrete specimens and, therefore, the elimination of scatter through unintentional specimen production or handling differences. Flexural strength measurements used wet-stored prisms at the ages of 2 d and 28 d, as well as dry-stored prisms at the ages of 28 d and 98 d. Fig. 4 shows the results of flexural and compressive strength tests.

Strength tests at the ages of 2 d and 28 d yield a nonlinear relationship between flexural and compressive strength (compare [57, 60]). Deviations from this trend are small and independent of concrete composition. This is confirmed for specimens tested at the ages of 28 d and 98 d, however, with an increased scatter. In contrast to early testing ages, strength increase is small, as also illustrated in Fig. 1.

3.5. Shrinkage

Concrete shrinkage comprises different components, with drying shrinkage induced through the loss of evaporable water being its major component [57]. For normal strength concrete, basic shrinkage as a consequence of cement hydration is several magnitudes smaller and therefore negligible [61]. In the present research, specimens were stored at 100 % r.h. until the age of 7 d, to further exclude an influence of basic shrinkage on measured deformations.

Fig. 5 illustrates the temporal development of shrinkage deformations ε_{cs} up to a concrete age of 98 d. As the difference between deformations at a concrete age of 1 d and 7 d is not uniform and also smaller than the standard deviation of three prisms, the assumption to neglect basic shrinkage seems justified. Therefore, the shrinkage development ε_{cs} starting at $t_s = 7$ d corresponds to the drying shrinkage.

The assessment of shrinkage deformations is generally impeded by a high scatter, especially in the present case of discontinuous measurements. [57] gives a coefficient of variation of 30 % for its model, which was partially adopted here to broaden the analytical

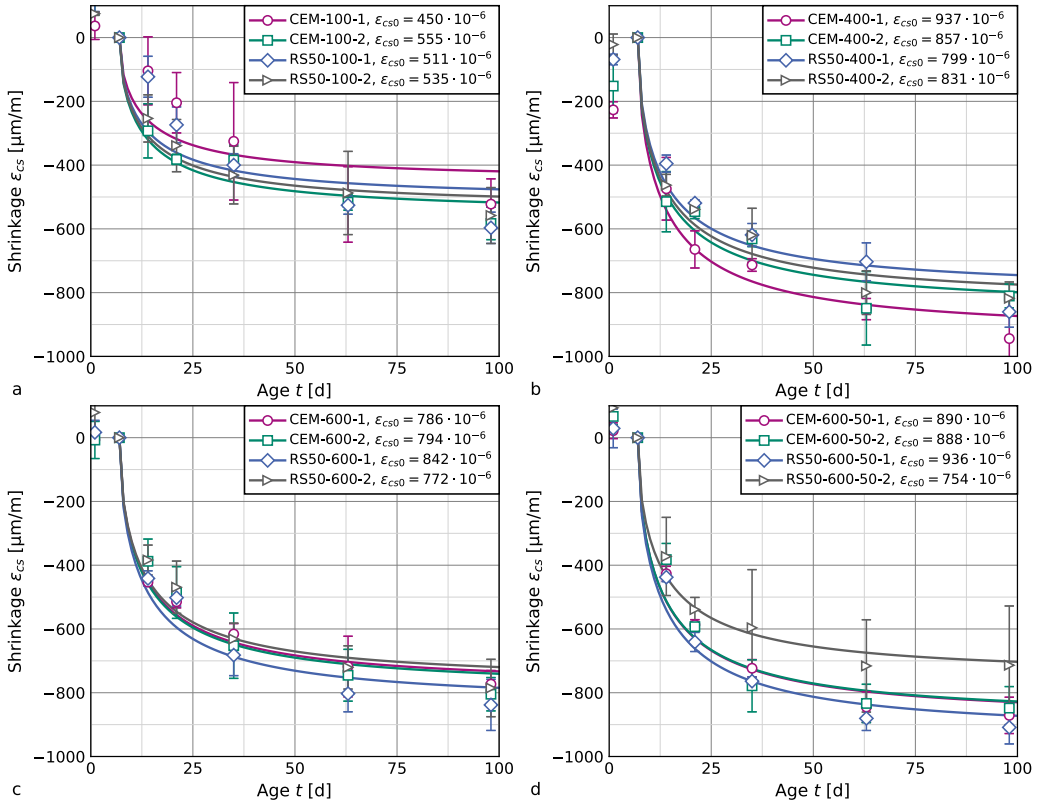

Fig. 5. Shrinkage deformation development for concrete mixes containing artificial fines "CEM" and "RS50", processed at different temperatures and with different substitution rates. Averages and standard deviations from three prisms as well as individual fit curves Eq. (6).

database. Here, drying shrinkage development consists of a drying shrinkage coefficient, a humidity coefficient, and a time function. As humidity is an invariant in the present study, the model is facilitated to comprise the time function $\beta_{ds}(t-t_s)$ and the shrinkage coefficient ε_{cs0}, which denotes the ultimate shrinkage deformation for $t - t_s \to \infty$ (see Eq. (6)).

$$\varepsilon_{cds}(t, t_s) = -\varepsilon_{cs0} \cdot \beta_{ds}(t - t_s) \tag{6}$$

$$\beta_{ds}(t - t_s) = \left(\frac{t - t_s}{0.035 \cdot h^2 + (t - t_s)} \right)^{0.5} \tag{7}$$

Eq. (6) condenses all material-dependent properties into ε_{cs0}, while the time function $\beta_{ds}(t - t_s)$ is only affected by specimen geometry, which was not altered in the present study ($h = 20\,\text{mm}$). Thus, ε_{cs0} obtained from fitting Eq. (6) to the experimental data by means of the least-squares method allows for the assessment of cement substitution through processed artificial fines. As exemplified in Fig. 5, most series show a good fit. Only concrete series with artificial fines "CEM-100" and "RS50-100", which were processed at 100 °C instead of activation at higher temperatures, exhibit a systematically slower shrinkage deformation development. This results in a systematic underestimation of the absolute shrinkage deformations for these series by Eq. (6).

This also shows in Fig. 6, where ε_{cs0} is illustrated over the reference strength $f_{cm,ref}$ and the dynamic modulus of elasticity E_c. Compared to the two reference series without CEM I-substitution, shrinkage increases with the inclusion of thermally activated artificial fines, which is in line with findings in [38,40]. This effect is especially pronounced for paste fines (CEM, S0, FA0) and for GW50 with its high content of reactive silica. In other artificial fines, ground inert aggregates may serve as micro-aggregates, which impede shrinkage deformations due to their high stiffness. The comparison of ε_{cs0} and E_c instead of $f_{cm,ref}$ substantiates this hypothesis.

3.6. Porosity

While mercury intrusion porosimetry measurements were conducted on separately produced paste specimens rather than concrete, the results still allow for assessing the impact of porosity on compressive strength.

Results for the reference series CEM I-1 and CEM I-2 confirm the reduction of total porosity alongside increasing compressive strength due to a reduction of the water-cement ratio (see Fig. 7(a)).

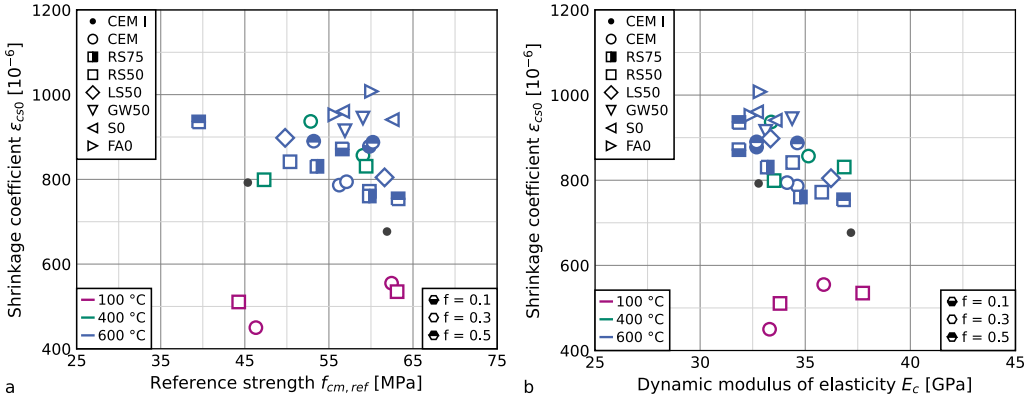

Fig. 6. Shrinkage coefficients ϵ_{cs0} over reference compressive strength $f_{cm,ref}$ (a), and dynamic moduli of elasticity E_c (b). Marker shapes indicate different artificial fines, fill styles indicate substitution rates (f), and color indicates processing temperatures.

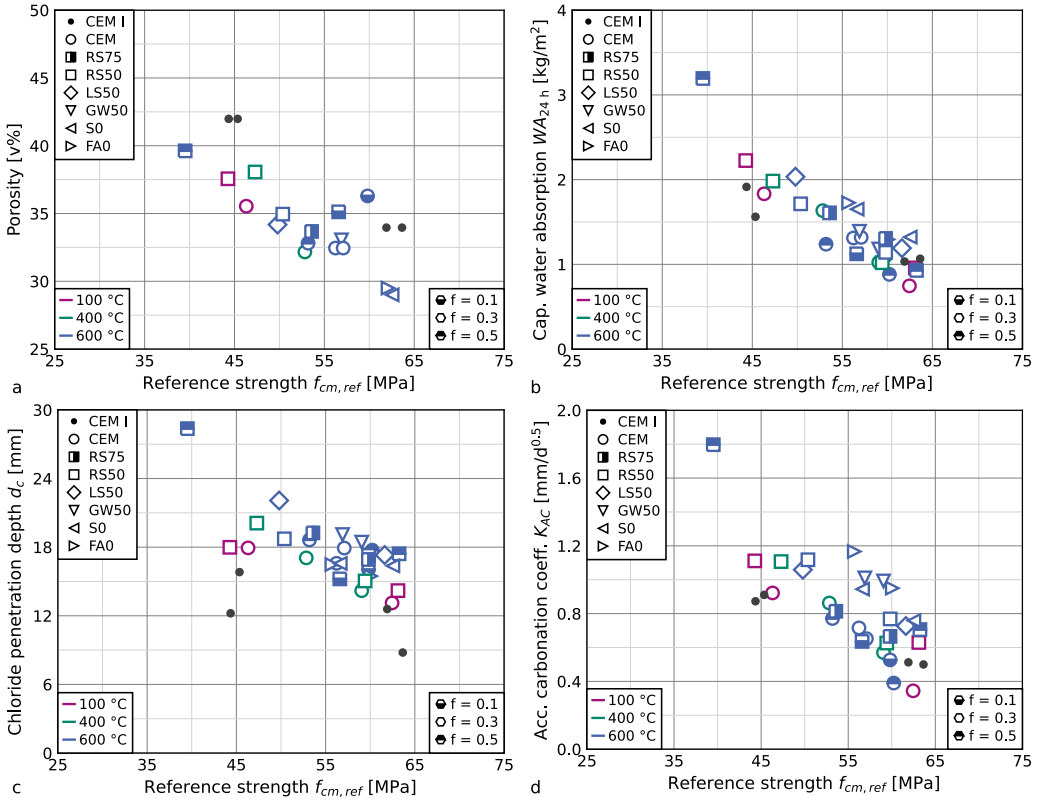

Fig. 7. Compressive strength dependency of different concrete durability parameters: Total porosity on paste specimens (a), capillary water absorption (b), chloride penetration depth (c), and accelerated carbonation coefficient (d). Marker shapes indicate artificial fines type and substitution rate, and marker colors indicate artificial fines activation temperature for different water-binder ratios.

However, except for the two series, where only 10 wt% of CEM I was replaced, all other series exhibit reduced paste porosity in concrete of similar strength, with the offset appearing to be independent of fines composition and activation temperature. While total porosity comprises all measured pores greater than 2 µm, the illustration of pore radius (r_p) distributions in Fig. 8 reveals the effect of CEM I-substitution beyond the increase in the effective water-cement ratio.

The higher water content in CEM I-1 compared to CEM I-2 leads to a significantly increased amount of pores with $100\,\text{nm} < r_p < 1000\,\text{nm}$ and $r_p < 20\,\text{nm}$. When partially replacing CEM I through activated concrete fines, the total water-binder ratio remains constant, but the paste microstructure changes for the reduction in cement hydration products and the increase in small inert particles. Subsequently, the porosity of the remaining hydration products is only marginally altered. For artificial fines containing

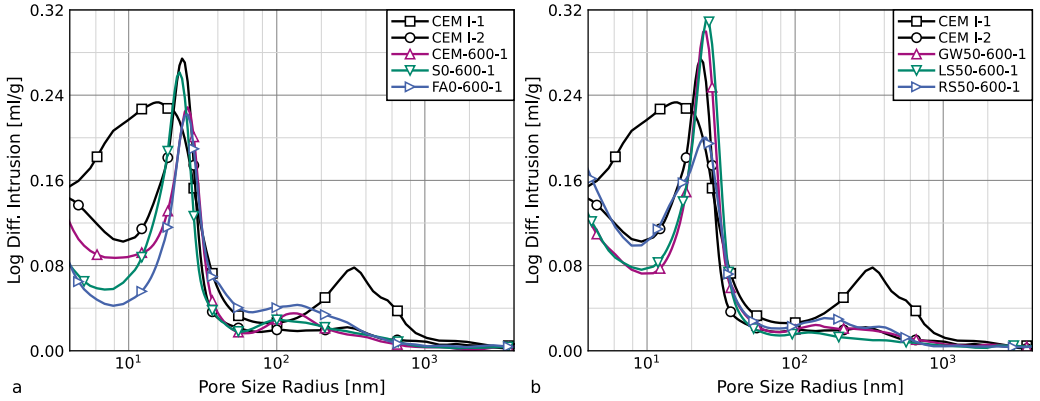

Fig. 8. Differential pore radius distribution (logarithmic) for reference series CEM I-1 and CEM I-2 as well as thermally activated artificial fines from pure paste (a), and artificial fines with different aggregate composition (b).

ground aggregates, this mostly affects pores with $r_p < 25\,\text{nm}$. Paste fines, which yield the highest concrete strength as SCM, have a similar decreasing effect on pores with $r_p < 25\,\text{nm}$, but at a higher magnitude. Conversely, porosity with $40\,\text{nm} < r_p < 200\,\text{nm}$ increases in comparison with artificial fines containing aggregates. This can be attributed to the reduction in w/b in the paste surrounding artificial fines particles due to the absorption, and consumption, of mixing water. This counteracts the higher internal porosity of these particles [25].

3.7. Capillary absorption

The effect of CEM I substitution through thermally activated artificial fines does not go beyond the reduction in compressive strength (Fig. 7(b)). When the reduction of strength is compensated for through reduced water-binder ratios, the water absorption coefficient $WA_{24\,\text{h}}$ also reduces, despite the increased total porosity. However, for low-strength concrete, water absorption is increased compared to the reference CEM I-1.

Capillary absorption interrelates with porosity, and no binding mechanisms can be expected. Fig. 9 illustrates the relationship between pore volume and capillary water absorption. Pore volume can be calculated directly from mercury intrusion measurements. As there is no consensus on a threshold for capillary activity, the definition in [37] was adopted, where harmful pores have a minimum radius (r_p) of 25 nm. Pores with a radius between 10 nm and 25 nm are considered "less harmful". Capillary suction decreases with increasing pore radius [62]. Therefore, an upper threshold of 1000 nm was chosen. Results in Fig. 8 exhibit nearly identical results for $r_p > 1000\,\text{nm}$. The results in Fig. 9 show that for a lower pore radius of 25 nm, water absorption of concrete mixes containing the artificial fines "CEM", "FA0", or "S0", which consist of pure cement paste with different binder compositions, agrees with interpolated results for the reference mixes CEM I-1 and -2. For the same pore volume, fines containing aggregates (RS75, RS50, and LS50) exhibit increased water absorption. Inert particles are surrounded by an interfacial transition zone (ITZ) with increased porosity, and for high concentrations of the particles, these ITZs may form a continuous network, which affects transport mechanisms beyond global porosity [62]. This hypothesis also explains the deviating behavior of RS50-600-50-1, which is the concrete mix with the highest amount of inert particles.

One notable exception is GW50, where aggregates are partly reactive and therefore might exhibit densified ITZs, resulting in reduced water absorption. Substantiating this hypothesis, however, requires elaborate microscopical analyses, like SEM, which were not part of the present experimental setup.

When including less harmful pores ($10\,\text{nm} < r_p < 25\,\text{nm}$) in the analysis (Fig. 9 b), the relationship between capillary absorption and pore volume is still observable, but disagrees with the reference mix CEM I-1. Therefore, the following analyses use a pore size of $r_p > 25\,\text{nm}$.

3.8. Chloride diffusion

Overall, regardless of compressive strength, chloride penetration depths d_c are increased, compared to the reference series without CEM I substitution. While the results for the artificial fines "CEM", consisting of pure CEM I-paste, are similar to the repetition of the reference series, which agrees with [43], results for other types of artificial fines exhibit an increased chloride penetration depth. Fig. 7(c) highlights individual magnitudes of this effect in connection with fines composition and processing.

Chloride diffusion is affected by interacting concrete properties, such as the w/b ratio, the degree of hydration, and pore structure [63]. Furthermore, chlorides may be chemically bound by cement hydration products, with aluminous compounds providing the highest binding capacity [62,64]. Fig. 10 illustrates individual mechanisms. In Fig. 10 a, chloride penetration depths of concrete with constant w/b ("–1") are plotted over paste pore volume. The results show a weak, but noticeable correlation

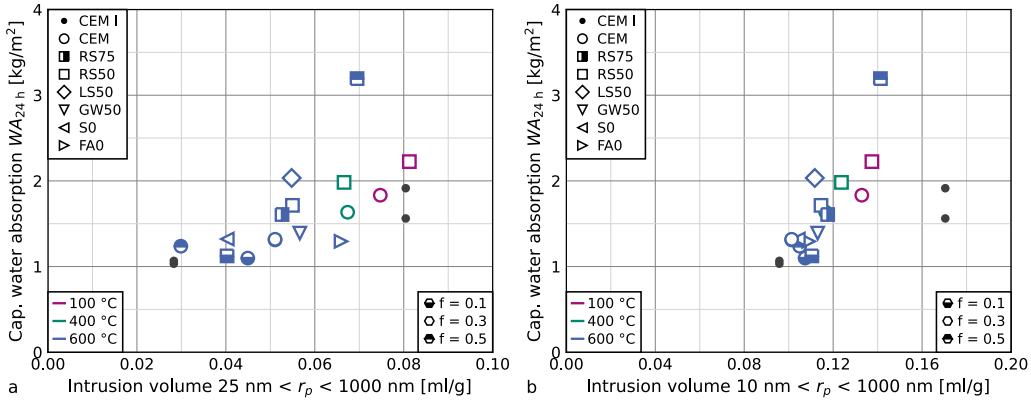

Fig. 9. Influence of pore volume for pore radius $25\,\text{nm} < r_p < 1000\,\text{nm}$ (a) and $5\,\text{nm} < r_p < 1000\,\text{nm}$ (b) of reference mixes and concrete mixes with constant w/b ("−1") on the capillary water absorption coefficient WA_{24}. Marker shapes indicate artificial fines type and substitution rate, and marker colors indicate artificial fines activation temperature for different water-binder ratios.

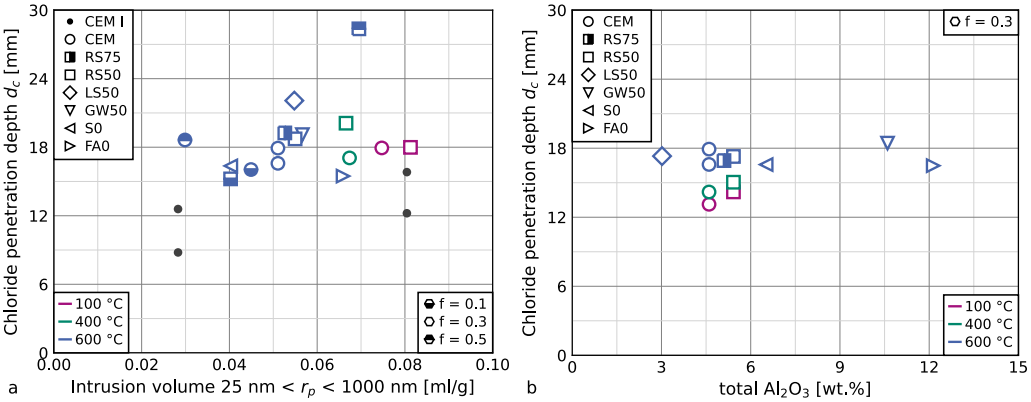

Fig. 10. Influence of pore volume of reference mixes and concrete mixes with constant w/b ("−1") (a) and influence of Al_2O_3-content in processed artificial fines in concrete mixes with constant w/c_{eq} ("−2") (b) on chloride penetration depth d_c. Marker shapes indicate artificial fines type and substitution rate, and marker colors indicate artificial fines activation temperature for different water-binder ratios.

between both parameters (compare [31,48,65]). In [31], the authors report an impact of open porosity between processed fines and OPC-paste, similar to capillary absorption, which further explains the present results.

Similar to capillary absorption, this trend is affected by artificial fines composition, where paste fines ("CEM", "FA0", "S0") exhibit lower penetration depths at similar porosity. Fig. 10 b illustrates the chloride penetration depth of concrete of the same target strength ("-2) over the total amount of Al_2O_3 in artificial fines, obtained from WDXRF-measurements (Table A.6). While fines processed at 600 °C exhibit similar penetration depths, regardless of fines composition, Fig. 10 b highlights the influence of the processing temperature. Artificial fines "CEM" and "RS50" exhibit a reduced penetration depth after processing at 400 °C or 100 °C, which suggests microstructural changes in these fines. [25] reports that sulfo-aluminates, which are a major contributor to chloride binding, carbonate easily. This agrees with findings in [47], where the chloride binding capacity increases when the activation temperature exceeds 800 °C, at which carbonates are essentially disintegrated. Accordingly, the concrete mix "CEM-100-2" exhibits the lowest chloride penetration depth of all mixes containing processed artificial fines. Here, essentially, CEM-100 substitutes CEM I and water, so that the newly formed paste and CEM-100 have a similar composition.

Regardless, these findings should be regarded with caution, as the repetition accuracy of the results must be considered. Presently, the double determination of CEM-600 yields a difference of $\Delta d_c = 1.3\,\text{mm}$ despite being produced on the same day from the same batches of raw materials. Even more, the repetition of CEM I-1 and CEM I-2 exhibits a difference of $\Delta d_c = 3.7\,\text{mm}$. In contrast to CEM-600, these series were produced with a temporal difference of three months. However, all results lie within the precision estimates for repeatability (CEM-600) or reproducibility (CEM I), detailed in EN 12390-11:2015 and EN 12390-18:2018.

3.9. Carbonation

Similar to chloride diffusion, concrete carbonation is enhanced by the partial replacement of CEM I, but also shows the individual impact of different fines composition and processing (see Fig. 7(d)).

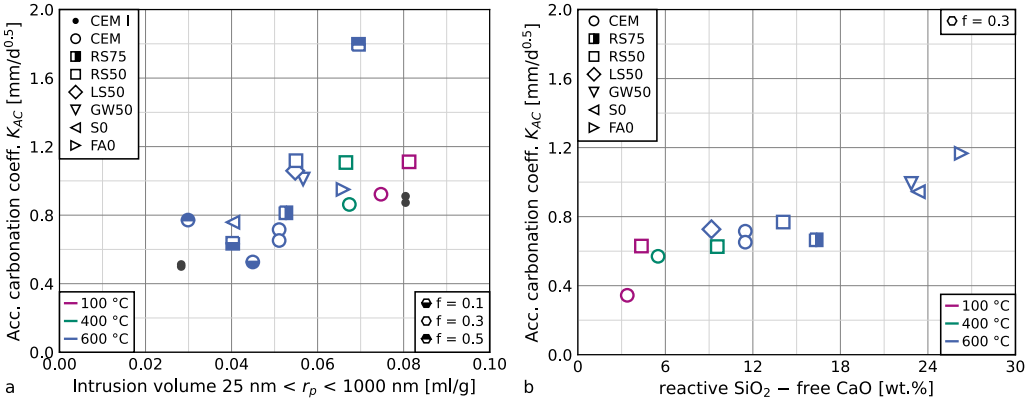

Fig. 11. Influence of pore volume of reference mixes and concrete mixes with constant w/b ("−1") (a) and influence of the chemical composition, represented through the difference in reactive SiO_2 and free CaO, in processed artificial fines in concrete mixes with constant w/c_{eq} ("−2") (b) on the accelerated carbonation coefficient K_{AC}. Marker shapes indicate artificial fines type and substitution rate, and marker colors indicate artificial fines activation temperature for different water-binder ratios.

The partial substitution of CEM I through processed CEM only affects carbonation alongside compressive strength reduction. Regardless of the processing temperature, K_{AC} follows the same relationship as the reference series CEM I-1 and CEM I-2. This may be caused by the binding of CO_2 in $Ca(OH)_2$. CEM-100 is essentially hydrated CEM I and therefore contains the same amount of $Ca(OH)_2$. During thermal activation, the hydration partially reverses, but upon rehydration, new $Ca(OH)_2$ forms. On the other hand, the amount of $Ca(OH)_2$ is reduced by fines with a high content of reactive SiO_2, which consumed the former for a pozzolanic reaction. Fig. 11 b exemplifies this behavior for concrete mixes with similar strength ("−2") by plotting the accelerated carbonation coefficient K_{AC} over the difference between reactive SiO_2 and free CaO. Subsequently, this exemplifies that even after compensating for compressive strength through adapting w/b, the fines composition impacts the carbonation behavior, which substantiates a hypothesis in [31]. Paste pore volume exhibits an additional influence on carbonation, which is similar to that of compressive strength. Fig. 11 a shows an increase of K_{AC} with higher pore volume. Here, concrete mixes without strength compensation ("−1") containing CEM regardless of the processing temperature follow the trend line set up by the reference mixes with pure CEM I. Fines with a reduced CaO- or increased SiO_2-content exhibit higher carbonation coefficients. These observations agree with results reported in [43], where the substitution of CEM I through activated cement paste has no effect on carbonation for substitution rates up to 30 wt%, whereas activated concrete fines containing inert particles increase carbonation depth. In comparison with chloride penetration, carbonation is affected to a larger extent by porosity, which was found to be caused by the semi-dry conditioning, whereas for chloride penetration, specimens are saturated [31].

3.10. Freeze-thaw-cycles

Due to the limited volume of the testing device, the effect of freeze-thaw-cycles on concrete containing processed artificial fines could only be investigated for mixes with $w/c_{eq} \approx 0.5$, so that the influence of diverging compressive strength can be ruled out from the interpretation of the results.

Fig. 12 illustrates the development of the mass loss with increasing number of freeze-thaw-cycles (FCT). For both presented types of artificial fines, "CEM-600" and "RS50-600", the substitution of 10 wt% CEM I has no effect on the mass loss after 56 FTC. For both SCMs, the substitution of 30 wt% CEM I increases the mass loss, while a higher substitution (50 wt%) has the adverse effect. This trend follows the capillary water absorption coefficient $WA_{24\,h}$, which was only evaluated up to 28 FCT (see Fig. 13).

After 28 FTC, the mass loss of the reference CEM I-2 is surpassed by half of the concrete mixes containing processed artificial fines. Generally, mass loss increases with higher water absorption, regardless of CEM I-substitution (compare [66]). As capillary absorption was not measured for series "−2", an influence of the latter cannot be derived from the data, but remains possible, especially since superplasticisers are known to refine porosity, and CEM-600-50 and RS50-600-50 required the highest amounts for a good workability (see Table A.5) [43].

4. Conclusion

For the design of durable concrete structures, compressive strength remains the most important material parameter, on which design codes are based. However, when sustainability requires the substitution of Portland cement (CEM I) through supplementary cementitious materials (SCMs), this may affect concrete compressive strength and other mechanical parameters as well as durability in different magnitudes, so that the applicability of established building codes may be compromised. The present study, therefore, used seven thermally activated artificial fines with different compositions, including binder type, aggregate content, and composition, as SCMs. The assessment of mechanical properties, as well as durability, included the production of two different

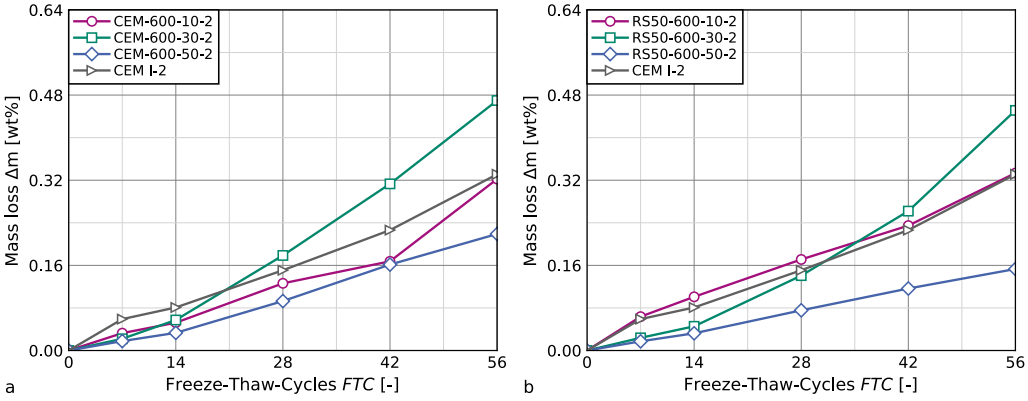

Fig. 12. Development of the cumulative mass loss after increasing freeze-thaw-cycles of concrete mixes containing 0 wt%-50 wt% CEM-600 (a) or RS50-600 (b) as CEM I-substitute.

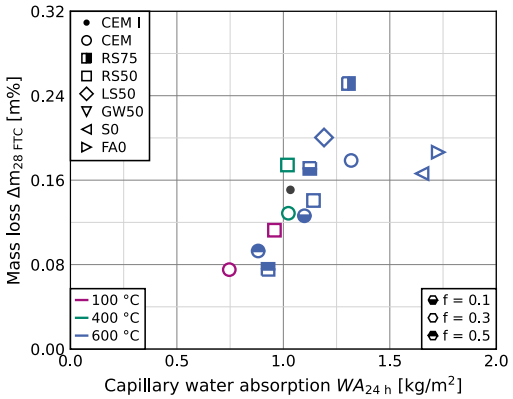

Fig. 13. Cumulative mass loss $\Delta m_{28\ FCT}$ and capillary water absorption coefficient $WA_{24\,h}$ of different concrete mixes with similar strength (series "−2"). Marker shapes indicate artificial fines type and substitution rate, and marker colors indicate artificial fines activation temperature for different water-binder ratios.

concrete mixes for each SCM with different compressive strengths. This enabled the assessment of whether the substitution of CEM I through activated artificial fines compromises concrete properties beyond compressive strength.

- Concrete compressive strength generally reduces when CEM I is partially substituted with processed artificial concrete fines. This can be compensated for by the reduction of the water-binder ratio following the *k*-value concept in EN 206:2021.
- Concrete containing processed fines exhibits a fast compressive strength development, which is similar to or exceeds the strength development of CEM I-concrete.
- Flexural strength of concrete containing processed fines changes alongside compressive strength, and follows the same relationship as CEM I-concrete.
- The dynamic modulus of elasticity and shrinkage are affected by the amount of inert particles contained in activated fines. A higher amount of inert particles reduces concrete deformations.
- While the total porosity of concrete at similar strength reduces with CEM I-replacement, the substitution negatively affects the resistance to chloride penetration and carbonation. This may have been caused by the reduced amount of cement hydration products, which can chemically bind chlorides and CO_2.
- Capillary water absorption of concrete containing processed fines follows the same dependence on compressive strength as CEM I-concrete. The freeze-thaw-resistance increases with higher water absorption.

In conclusion, the present results show that concrete with a CEM I substitution through up to 50 wt% thermally activated artificial fines exhibits a good mechanical behavior. Therefore, existing building standards and their underlying empirical relationships between compressive strength and other mechanical properties are applicable to estimate the long-term behavior of concrete containing activated fines as SCM.

However, especially for the mostly negative influence of activated fines on concrete durability, additional research, e.g., through SEM-EDS is required, where the effect of CEM I substitution on microstructure and the binding capacity of hydration products is

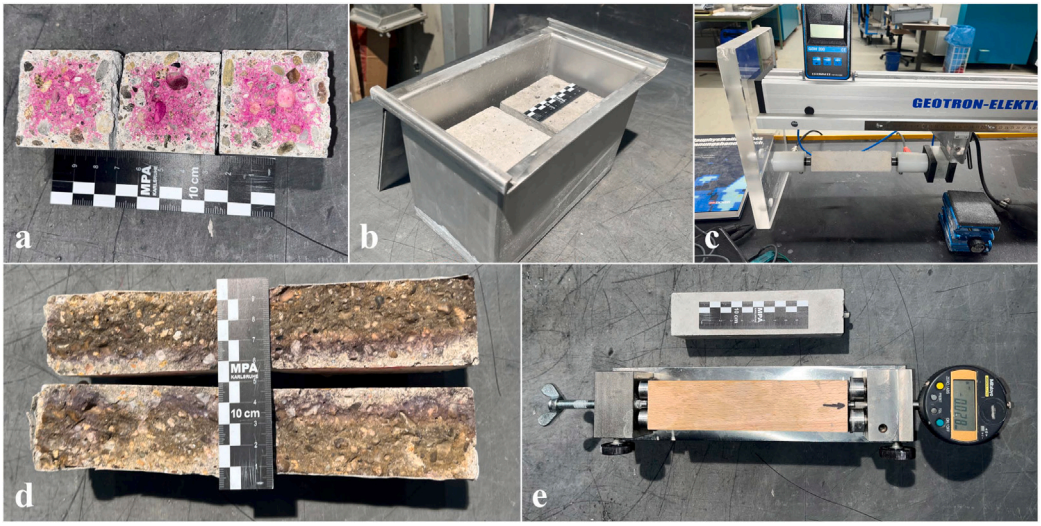

Fig. A.14. Photographic illustration of the test setups. (a): split prisms with phenolphtailein, indicating carbonation depth. (b): cubes in freeze-thaw container. (c): prism in ultrasonic pulse applicator. (d): split cylinders with silver nitrate, indicating chloride penetration. (e): shrinkage strain gauge with calibration rod.

linked to corrosive processes. The results highlight that a more thorough understanding of these processes is necessary, similar to more established SCMs, as presented in [67,68]. Ultimately, additional research needs to translate the present findings to recycled concrete fines from industrial sources and include a broader dataset to statistically secure the findings.

CRediT authorship contribution statement

Jan P. Höffgen: Writing – original draft, Visualization, Methodology, Funding acquisition, Formal analysis, Conceptualization. **Marius Schmitt:** Writing – review & editing, Formal analysis. **Frank Dehn:** Writing – review & editing, Supervision, Project administration, Funding acquisition.

Declaration of Generative AI and AI-assisted technologies in the writing process

During the preparation of this work, the authors used Grammarly and DeepL in order to check for spelling and wording errors. After using these tools/services, the authors reviewed and edited the content as needed and take full responsibility for the content of the published article.

Funding

This work was supported by the Dres. Edith und Klaus Dyckerhoff-Stiftung, grant no. T0218/36374.

Declaration of competing interest

The authors declare that they have no known competing financial interests or personal relationships that could have appeared to influence the work reported in this paper.

Appendix

See Table A.5, Table A.6, Fig. A.14, Fig. A.15 and Fig. A.16.

Data availability

Data will be made available on request.

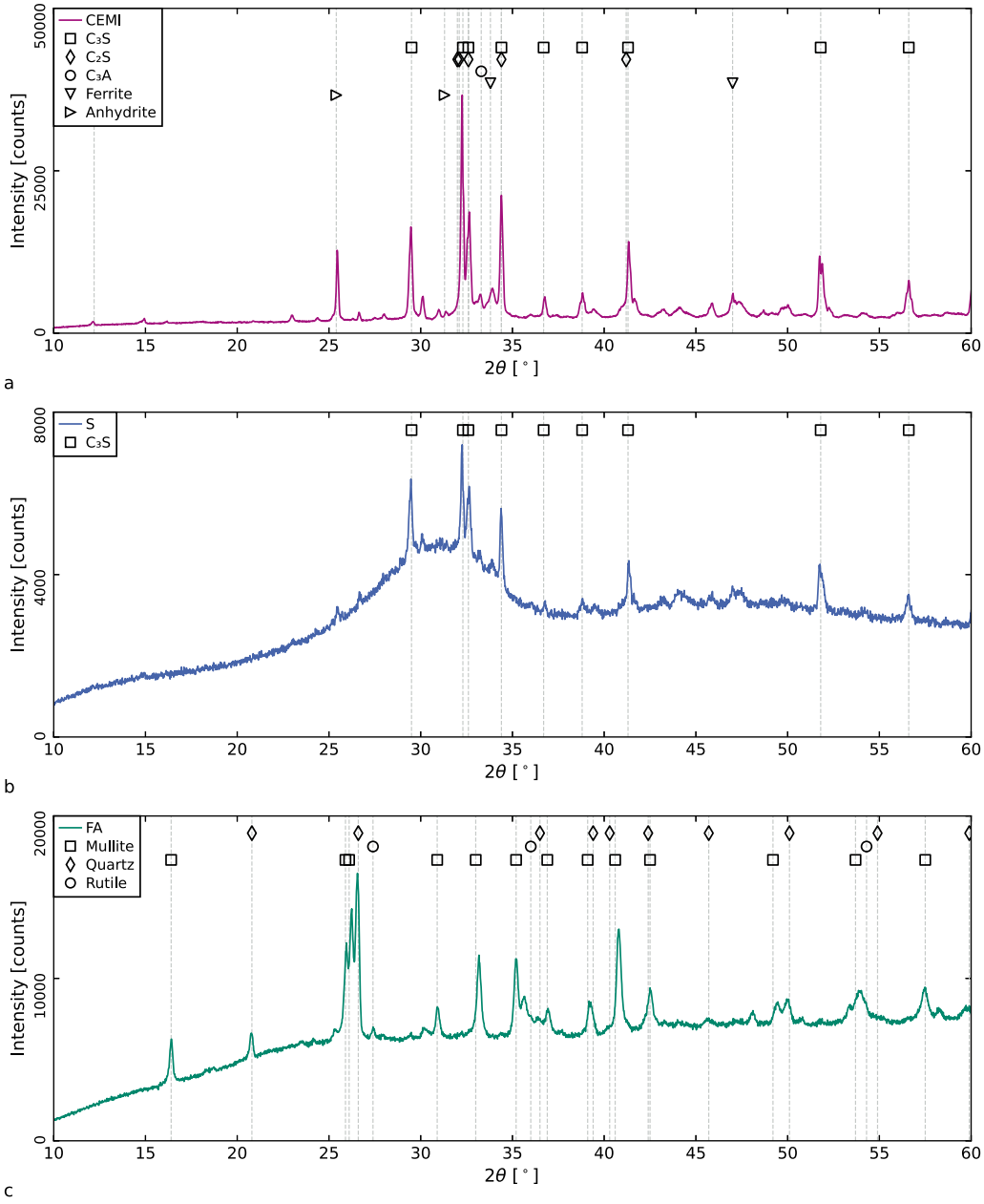

Fig. A.15. Qualitative X-ray Diffraction (XRD) of binders. (a): CEM I, (b): Slag (S), (c): Fly Ash (FA).

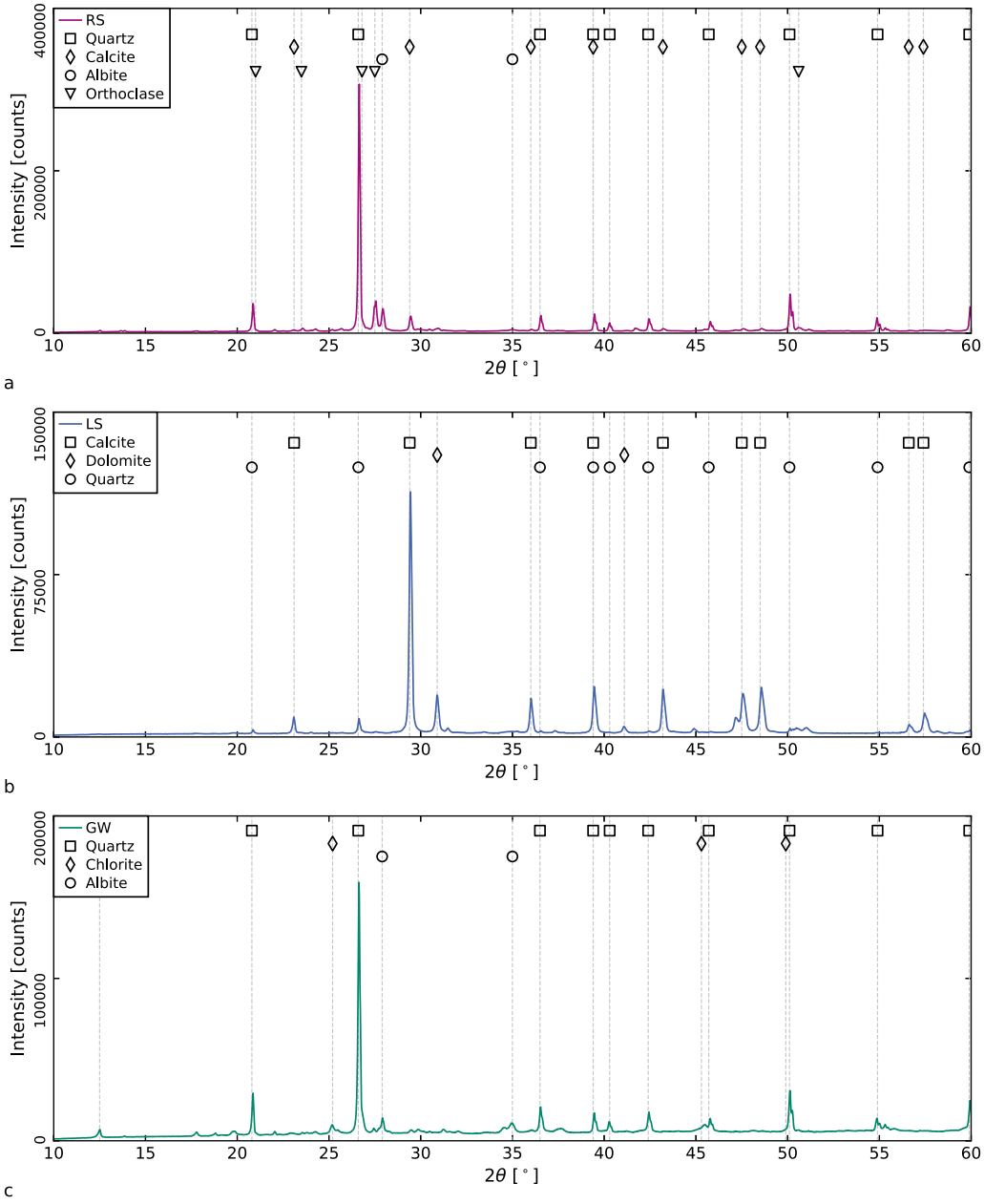

Fig. A.16. Qualitative X-ray Diffraction (XRD) of aggregates. (a): River Sand (RS), (b): Limestone (LS), (c): Greywacke (GW).

Table A.5
Overview of different series. SCM: supplementary cementitious material. f: substitution rate of CEM I through SCM. k: assumed k-value. w/b: selected water-binder ratio. w/c_{eq}: resulting equivalent water-cement ratio. w: water content. c: CEM I content. a: SCM content. SP: superplasticizer dosage for achieving target consistency. Aggregate content for all series: RS: 526 kg/m^3, RG: 1024 kg/m^3.

Series	SCM	f –	k –	w/b –	w/c_{eq} –	w kg/m^3	c kg/m^3	a kg/m^3	SP kg/m^3
CEM I-1	CEM I	0.0		0.60	0.60	261	435		0.0
CEM I-2				0.50	0.50	244	488		0.0
CEM-100-1	CEM-100	0.3	0.20	0.50	0.66	235	329	141	2.3
CEM-100-2				0.38	0.50	208	383	164	8.2
CEM-400-1	CEM-400	0.3	0.66	0.50	0.56	236	331	142	3.5
CEM-400-2				0.45	0.50	226	352	151	4.3
CEM-600-1	CEM-600	0.3	1.00	0.50	0.50	239	335	144	3.2
CEM-600-2				0.50	0.50	239	335	144	3.6
CEM-600-10-2		0.1	1.00	0.50	0.50	243	437	49	0.0
CEM-600-50-1		0.5	0.80	0.50	0.56	237	237	237	7.0
CEM-600-50-2				0.45	0.50	226	251	251	12.7
FA0-600-1	FA0-600	0.3	1.20	0.50	0.47	240	336	144	1.6
FA0-600-2				0.53	0.50	245	324	139	0.8
S0-600-1	S0-600	0.3	1.20	0.50	0.47	240	337	144	1.7
S0-600-2				0.53	0.50	246	325	139	0.6
RS75-600-1	RS75-600	0.3	0.84	0.50	0.53	240	337	144	1.3
RS75-600-2				0.47	0.49	234	349	150	2.1
RS50-100-1	RS50-100	0.3	0.25	0.50	0.65	238	333	143	0.0
RS50-100-2				0.39	0.50	213	383	164	4.0
RS50-400-1	RS50-400	0.3	0.46	0.50	0.60	238	334	143	1.2
RS50-400-2				0.41	0.49	219	374	160	4.7
RS50-600-1	RS50-600	0.3	0.50	0.50	0.59	238	334	143	1.2
RS50-600-2				0.43	0.49	224	364	156	3.4
RS50-600-10-2		0.1	1.00	0.50	0.50	242	436	48	0.0
RS50-600-50-1		0.5	0.40	0.50	0.71	235	235	235	3.5
RS50-600-50-2				0.35	0.50	199	285	285	10.0
LS50-600-1	LS50-600	0.3	0.51	0.50	0.59	240	336	144	1.2
LS50-600-2				0.43	0.50	225	367	157	3.4
GW50-600-1	GW50-600	0.3	0.80	0.50	0.53	240	336	144	1.2
GW50-600-2				0.47	0.50	234	348	149	2.5

Table A.6
Chemical composition of the raw materials for concrete and artificial fines production through Wavelength Dispersive X-ray Fluorescence Spectroscopy (WDXRF) (EN 196-2:2013). LOI: Loss on ignition.

	Na_2O wt%	MgO wt%	Al_2O_3 wt%	SiO_2 wt%	P_2O_5 wt%	K_2O wt%	CaO wt%	TiO_2 wt%	MnO wt%	Fe_2O_3 wt%	LOI wt%
CEM I	0.1	1.9	4.6	19.8	0.2	0.8	60.7	0.2	0.2	3.2	2.4
S	0.2	5.6	11.0	35.7	0.1	0.7	41.6	1.0	0.6	1.3	−1.0
FA	0.4	1.3	29.7	48.1	0.3	1.3	3.1	3.4	0.1	9.2	1.8
RS	1.2	0.6	5.8	80.6	0.1	2.0	4.1	0.1	0.0	1.1	3.8
LS	0.0	3.0	2.3	7.7	0.1	0.8	44.3	0.1	0.0	0.9	38.5
GW	0.8	1.9	13.3	68.8	0.1	3.1	1.1	0.9	0.1	5.4	3.8

References

[1] J.H. Aquino Rocha, R.D. Toledo Filho, The utilization of recycled concrete powder as supplementary cementitious material in cement-based materials: A systematic literature review, J. Build. Eng. 76 (2023) 107319, http://dx.doi.org/10.1016/j.jobe.2023.107319.

[2] A. Carriço, J.A. Bogas, M. Guedes, Thermoactivated cementitious materials – A review, Constr. Build. Mater. 250 (2020) 118873, http://dx.doi.org/10.1016/j.conbuildmat.2020.118873.

[3] Z. He, X. Zhu, J. Wang, M. Mu, Y. Wang, Comparison of CO2 emissions from OPC and recycled cement production, Constr. Build. Mater. 211 (2019) 965–973, http://dx.doi.org/10.1016/j.conbuildmat.2019.03.289.

[4] E.A. Ohemeng, S.O. Ekolu, A review on the reactivation of hardened cement paste and treatment of recycled aggregates, Mag. Concr. Res. 72 (10) (2020) 526–539, http://dx.doi.org/10.1680/jmacr.18.00452.

[5] S. Real, V. Sousa, I. Meireles, J.A. Bogas, A. Carriço, Life Cycle Assessment of Thermoactivated Recycled Cement Production, Mater. (Basel, Switzerland) 15 (19) (2022) http://dx.doi.org/10.3390/ma15196766.

[6] V. Sousa, J.A. Bogas, Comparison of energy consumption and carbon emissions from clinker and recycled cement production, J. Clean. Prod. 306 (2021) 127277, http://dx.doi.org/10.1016/j.jclepro.2021.127277.

[7] V. Sousa, J.A. Bogas, S. Real, I. Meireles, Industrial production of recycled cement: Energy consumption and carbon dioxide emission estimation, Environ. Sci. Pollut. Res. 30 (4) (2022) 8778–8789, http://dx.doi.org/10.1007/s11356-022-20887-7.

[8] V. Sousa, J.A. Bogas, S. Real, I. Meireles, A. Carriço, Recycled cement production energy consumption optimization, Sustain. Chem. Pharm. 32 (2023) 101010, http://dx.doi.org/10.1016/j.scp.2023.101010.

[9] L. Xu, J. Wang, K. Li, S. Lin, M. Li, T. Hao, Z. Ling, D. Xiang, T. Wang, A systematic review of factors affecting properties of thermal-activated recycled cement, Resour. Conserv. Recycl. 185 (2022) 106432, http://dx.doi.org/10.1016/j.resconrec.2022.106432.

[10] S.C. Angulo, M.S. Guilge, V.A. Quarcioni, M.A. Cincotto, T.R. Nobre, H. Pöllmann, The role of calcium silicates and quicklime on the reactivity of rehydrated cements, Constr. Build. Mater. 340 (2022) 127625, http://dx.doi.org/10.1016/j.conbuildmat.2022.127625.

[11] T.F. Baggio, E. Possan, J.J. De Oliveira Andrade, Physical-chemical characterization of construction and demolition waste powder with thermomechanical activation for use as supplementary cementitious material, Constr. Build. Mater. 437 (2024) 136907, http://dx.doi.org/10.1016/j.conbuildmat.2024.136907.

[12] R. Baldusco, T.R.S. Nobre, S.C. Angulo, V.A. Quarcioni, M.A. Cincotto, Dehydration and Rehydration of Blast Furnace Slag Cement, J. Mater. Civ. Eng. 31 (8) (2019) 04019132, http://dx.doi.org/10.1061/(ASCE)MT.1943-5533.0002725.

[13] J.A. Bogas, S. Real, A. Carriço, J. Abrantes, M. Guedes, Hydration and phase development of recycled cement, Cem. Concr. Compos. 127 (2022) 104405, http://dx.doi.org/10.1016/j.cemconcomp.2022.104405.

[14] A. Carriço, S. Real, J.A. Bogas, M.F. Costa Pereira, Mortars with thermo activated recycled cement: Fresh and mechanical characterisation, Constr. Build. Mater. 256 (2020) 119502, http://dx.doi.org/10.1016/j.conbuildmat.2020.119502.

[15] K. Kalinowska-Wichrowska, M. Kosior-Kazberuk, E. Pawluczuk, The Properties of Composites with Recycled Cement Mortar Used as a Supplementary Cementitious Material, Materials 13 (1) (2020) 64, http://dx.doi.org/10.3390/ma13010064.

[16] N. Noel, T. Mielke, G. Semugaza, A.Z. Gierth, S. Helmich, S. Nawrath, D.C. Lupascu, Chemical transformations during the preparation and rehydration of reactivated virgin cements, CEMENT 19 (2025) 100129, http://dx.doi.org/10.1016/j.cement.2025.100129.

[17] S. Real, A. Carriço, J.A. Bogas, M. Guedes, Influence of the Treatment Temperature on the Microstructure and Hydration Behavior of Thermoactivated Recycled Cement, Materials 13 (18) (2020) 3937, http://dx.doi.org/10.3390/ma13183937.

[18] G. Semugaza, T. Mielke, M.E. Castillo, A.Z. Gierth, J.X. Tam, S. Nawrath, D.C. Lupascu, Reactivation of hydrated cement powder by thermal treatment for partial replacement of ordinary portland cement, Mater. Struct. 56 (3) (2023) http://dx.doi.org/10.1617/s11527-023-02133-9.

[19] R. Serpell, M. Lopez, Properties of mortars produced with reactivated cementitious materials, Cem. Concr. Compos. 64 (2015) 16–26, http://dx.doi.org/10.1016/j.cemconcomp.2015.08.003.

[20] R. Serpell, F. Zunino, Recycling of hydrated cement pastes by synthesis of α'H-C2S, Cem. Concr. Res. 100 (2017) 398–412, http://dx.doi.org/10.1016/j.cemconres.2017.08.001.

[21] Y. Sui, C. Ou, S. Liu, J. Zhang, Q. Tian, Study on Properties of Waste Concrete Powder by Thermal Treatment and Application in Mortar, Appl. Sci. 10 (3) (2020) 998, http://dx.doi.org/10.3390/app10030998.

[22] E. Tajuelo Rodriguez, K. Garbev, D. Merz, L. Black, I.G. Richardson, Thermal stability of C-S-H phases and applicability of Richardson and Groves' and Richardson C-(A)-S-H(I) models to synthetic C-S-H, Cem. Concr. Res. 93 (2017) 45–56, http://dx.doi.org/10.1016/j.cemconres.2016.12.005.

[23] J. Zelic, L. Ugrina, D. Jozic, Application of Thermal Methods in the Chemistry of Cement: Kinetic Analysis of Portlandite from Non-Isothermal Thermogravimetric Data, in: The First International Proficiency Testing Conference, n. d., Sinaia, Romania, 2007, pp. 420–429.

[24] J.A. Bogas, A. Carriço, M. Pereira, Mechanical characterization of thermal activated low-carbon recycled cement mortars, J. Clean. Prod. 218 (2019) 377–389, http://dx.doi.org/10.1016/j.jclepro.2019.01.325.

[25] J.A. Bogas, A. Carriço, A.J. Tenza-Abril, Microstructure of thermoactivated recycled cement pastes, Cem. Concr. Res. 138 (2020) 106226, http://dx.doi.org/10.1016/j.cemconres.2020.106226.

[26] Z. Shui, D. Xuan, H. Wan, B. Cao, Rehydration reactivity of recycled mortar from concrete waste experienced to thermal treatment, Constr. Build. Mater. 22 (8) (2008) 1723–1729, http://dx.doi.org/10.1016/j.conbuildmat.2007.05.012.

[27] X. Xi, Y. Zheng, C. Du, P. Zhang, M. Sun, Study on the hydration characteristics, mechanical properties, and microstructure of thermally activated low-carbon recycled cement, Constr. Build. Mater. 447 (2024) 138042, http://dx.doi.org/10.1016/j.conbuildmat.2024.138042.

[28] J. Kim, N. Kim, Exploring the role of thermal activation of cement exposed to the external environment on the improvement of concrete properties, J. Mater. Res. Technol. 24 (2023) 2868–2878, http://dx.doi.org/10.1016/j.jmrt.2023.03.195.

[29] D. Qian, R. Yu, Z. Shui, Y. Sun, C. Jiang, F. Zhou, M. Ding, X. Tong, Y. He, A novel development of green ultra-high performance concrete (UHPC) based on appropriate application of recycled cementitious material, J. Clean. Prod. 261 (2020) 121231, http://dx.doi.org/10.1016/j.jclepro.2020.121231.

[30] Z. Shui, D. Xuan, W. Chen, R. Yu, R. Zhang, Cementitious characteristics of hydrated cement paste subjected to various dehydration temperatures, Constr. Build. Mater. 23 (1) (2009) 531–537, http://dx.doi.org/10.1016/j.conbuildmat.2007.10.016.

[31] J.A. Bogas, A. Carriço, S. Real, Durability of concrete produced with recycled cement from waste concrete, 3rd International Congress on Materials & Structural Stability, Mater. Today: Proc. 58 (2022) 1149–1154, http://dx.doi.org/10.1016/j.matpr.2022.01.280.

[32] V. Letelier, E. Tarela, P. Muñoz, G. Moriconi, Combined effects of recycled hydrated cement and recycled aggregates on the mechanical properties of concrete, Constr. Build. Mater. 132 (2017) 365–375, http://dx.doi.org/10.1016/j.conbuildmat.2016.12.010.

[33] Z. Ma, J. Shen, H. Wu, P. Zhang, Properties and activation modification of eco-friendly cementitious materials incorporating high-volume hydrated cement powder from construction waste, Constr. Build. Mater. 316 (2022) 125788, http://dx.doi.org/10.1016/j.conbuildmat.2021.125788.

[34] A. Tokareva, S. Kaassamani, D. Waldmann, Fine demolition wastes as Supplementary cementitious materials for CO2 reduced cement production, Constr. Build. Mater. 392 (2023) 131991, http://dx.doi.org/10.1016/j.conbuildmat.2023.131991.

[35] P. Vashistha, Y. Oinam, H.-K. Kim, S. Pyo, Effect of thermo-mechanical activation of waste concrete powder (WCP) on the characteristics of cement mixtures, Constr. Build. Mater. 362 (2023) 129713, http://dx.doi.org/10.1016/j.conbuildmat.2022.129713.

[36] H. Wu, C. Liang, Z. Zhang, P. Yao, C. Wang, Z. Ma, Utilizing heat treatment for making low-quality recycled aggregate into enhanced recycled aggregate, recycled cement and their fully recycled concrete, Constr. Build. Mater. 394 (2023) 132126, http://dx.doi.org/10.1016/j.conbuildmat.2023.132126.

[37] M. Wei, L. Chen, N. Lei, H. Li, L. Huang, Mechanical properties and microstructures of thermally activated ultrafine recycled fine powder cementitious materials, Constr. Build. Mater. 475 (2025) 141195, http://dx.doi.org/10.1016/j.conbuildmat.2025.141195.

[38] S. Real, J.A. Bogas, A. Carriço, S. Hu, Mechanical Characterisation and Shrinkage of Thermoactivated Recycled Cement Concrete, Appl. Sci. 11 (6) (2021) 2454, http://dx.doi.org/10.3390/app11062454.

[39] E.M. Getachew, B.W. Yifru, B.T. Habtegebreal, M.D. Yehualaw, Performance evaluation of mortar with ground and thermo-activated recycled concrete cement, Cogent Eng. 11 (1) (2024) 2357726, http://dx.doi.org/10.1080/23311916.2024.2357726.

[40] A. Carriço, J.A. Bogas, S. Real, M.F.C. Pereira, Shrinkage and sorptivity of mortars with thermoactivated recycled cement, Constr. Build. Mater. 333 (2022) 127392, http://dx.doi.org/10.1016/j.conbuildmat.2022.127392.

[41] J. Kim, A. Ubysz, Thermal activation of multi-recycled concrete powder as supplementary cementitious material for repeated and waste-free recycling, J. Build. Eng. 98 (2024) 111169, http://dx.doi.org/10.1016/j.jobe.2024.111169.

[42] A. Tokareva, D. Waldmann, Durability of cement mortars containing fine demolition wastes as supplementary cementitious materials, Constr. Build. Mater. 477 (2025) 141316, http://dx.doi.org/10.1016/j.conbuildmat.2025.141316.

[43] A. Carriço, S. Real, J.A. Bogas, Durability performance of thermoactivated recycled cement concrete, Cem. Concr. Compos. 124 (2021) http://dx.doi.org/10.1016/j.cemconcomp.2021.104270.

[44] H. Wu, D. Yang, Z. Ma, Micro-structure, mechanical and transport properties of cementitious materials with high-volume waste concrete powder and thermal modification, Constr. Build. Mater. 313 (2021) 125477, http://dx.doi.org/10.1016/j.conbuildmat.2021.125477.
[45] N. Algourdin, Q. Nguyen, Z. Mesticou, A. Si Larbi, Durability of recycled fine mortars under freeze–thaw cycles, Constr. Build. Mater. 291 (2021) 123330, http://dx.doi.org/10.1016/j.conbuildmat.2021.123330.
[46] M. Wei, L. Chen, N. Lei, H. Li, L. Huang, Experimental investigation on freeze–thaw resistance of thermally activated recycled fine powder concrete, Constr. Build. Mater. 457 (2024) 139378, http://dx.doi.org/10.1016/j.conbuildmat.2024.139378.
[47] Z. He, R. Hu, Z. Ma, X. Liu, C. Wang, H. Wu, Reusing thermoactivated construction waste spoil as sustainable binder for durable concrete: Microstructure and chloride transport, Constr. Build. Mater. 398 (2023) 132553, http://dx.doi.org/10.1016/j.conbuildmat.2023.132553.
[48] L. Xu, J. Wang, X. Hu, B. Ran, T. Wu, X. Zhou, Y. Xiong, Physical performance, durability, and carbon emissions of recycled cement concrete and fully recycled concrete, Constr. Build. Mater. 447 (2024) 138128, http://dx.doi.org/10.1016/j.conbuildmat.2024.138128.
[49] A. Carriço, J.A. Bogas, S. Hu, S. Real, M.F. Costa Pereira, Novel separation process for obtaining recycled cement and high-quality recycled sand from waste hardened concrete, J. Clean. Prod. 309 (2021) 127375, http://dx.doi.org/10.1016/j.jclepro.2021.127375.
[50] E.W. Klingsch, Explosive Spalling of Concrete in Fire (Ph.D. thesis), ETH Zurich, Zürich, 2014, http://dx.doi.org/10.3929/ethz-a-010243000.
[51] A. Lipowsky, A. Müller, Gesteinsmehl als Zuschlagstoffe in hydraulischen Bindemitteln, Aufbereitungs-Technik/Mineral Process. 58 (12) (2017) 52–64.
[52] R. Serpell, M. Lopez, Reactivated cementitious materials from hydrated cement paste wastes, Cem. Concr. Compos. 39 (2013) 104–114, http://dx.doi.org/10.1016/j.cemconcomp.2013.03.020.
[53] L. Xu, J. Wang, K. Li, M. Li, S. Lin, T. Hao, T. Wang, Y. Guo, Z. Ling, Investigations on the rehydration of recycled blended SCMs cement, Cem. Concr. Res. 163 (2023) 107036, http://dx.doi.org/10.1016/j.cemconres.2022.107036.
[54] L. Xu, J. Wang, K. Li, T. Hao, Z. Li, L. Li, B. Ran, H. Du, New insights on dehydration at elevated temperature and rehydration of GGBS blended cement, Cem. Concr. Compos. 139 (2023) 105068, http://dx.doi.org/10.1016/j.cemconcomp.2023.105068.
[55] J.P. Höffgen, F. Dehn, Influence of thermally activated artificial concrete fines composition on mortar strength development, Dev. the Built Environ. 24 (2025) 100775, http://dx.doi.org/10.1016/j.dibe.2025.100775.
[56] J.P. Höffgen, S. Bruckschlögl, B. Wetz, F. Dehn, Influence of thermally activated industrial concrete fines of different origin on mortar strength development, Case Stud. Constr. Mater. (2025) e05427, http://dx.doi.org/10.1016/j.cscm.2025.e05427.
[57] International Federation for Structural Concrete (Ed.), Fib model code for concrete structures (2020), Version 1, International Federation for Structural Concrete (fib), Lausanne, 2023.
[58] N. Ekin, O. Uyanik, Comparison of Static and Dynamic Elastic Moduli in Concrete: Effects of Compressive Strength, Curing Conditions and Reinforcement, Iran. J. Sci. Technol. Trans. Civ. Eng. 45 (4) (2021) 2327–2343, http://dx.doi.org/10.1007/s40996-020-00513-7.
[59] A.I. Marques, J. Morais, P. Morais, M.D.R. Veiga, C. Santos, P. Candeias, J.G. Ferreira, Modulus of elasticity of mortars: Static and dynamic analyses, Constr. Build. Mater. 232 (2020) 117216, http://dx.doi.org/10.1016/j.conbuildmat.2019.117216.
[60] R. Campos, M.M.M. Larrain, M. Zaman, V. Pozadas, Relationships between compressive and flexural strengths of concrete based on fresh field properties, Int. J. Pavement Res. Technol. 14 (2) (2021) 161–167, http://dx.doi.org/10.1007/s42947-020-1074-0.
[61] H.S. Müller, F. Acosta Urrea, V. Kvitsel, Modelle zur Vorhersage des Schwindens und Kriechens von Beton: Teil 1: Analyse des Schwindmodells in DIN EN 1992-1-1:2011 und neuer Ansatz im Eurocode 2 prEN 1992-1-1:2020, Beton- Und Stahlbetonbau 116 (1) (2021) 2–18, http://dx.doi.org/10.1002/best.202000082.
[62] F.W. Locher, Cement Principles of Production and Use, Verl. Bau und Technik, Düsseldorf, 2006.
[63] N. Ukrainczyk, T. Bernard, A. Babaahmadi, L. Huang, C. Zausinger, A. Soive, S. Bonnet, F. Georget, M. Mrak, S. Dolenec, T. Völker, P. Suraneni, W. Wilson, Test methods for chloride diffusivity of blended cement pastes: A review by RILEM TC 298-EBD, Mater. Struct. 58 (10) (2025) 324, http://dx.doi.org/10.1617/s11527-025-02809-4.
[64] K. De Weerdt, W. Wilson, A. Machner, F. Georget, Chloride profiles – What do they tell us and how should they be used? Cem. Concr. Res. 173 (2023) 107287, http://dx.doi.org/10.1016/j.cemconres.2023.107287.
[65] Y. Yang, R.A. Patel, S.V. Churakov, N.I. Prasianakis, G. Kosakowski, M. Wang, Multiscale modeling of ion diffusion in cement paste: Electrical double layer effects, Cem. Concr. Compos. 96 (2019) 55–65, http://dx.doi.org/10.1016/j.cemconcomp.2018.11.008.
[66] J. Stark, B. Wicht, Dauerhaftigkeit Von Beton, second ed., Springer-Verlag, Berlin, 2013, http://dx.doi.org/10.1077/978-3-642-35278-2.
[67] S. Greve-Dierfeld, B. Lothenbach, A. Vollpracht, B. Wu, B. Huet, C. Andrade, C. Medina, C. Thiel, E. Gruyaert, H. Vanoutrive, I.F. Del Saéz Bosque, I. Ignjatovic, J. Elsen, J.L. Provis, K. Scrivener, K.-C. Thienel, K. Sideris, M. Zajac, N. Alderete, Ö. Cizer, P. van den Heede, R.D. Hooton, S. Kamali-Bernard, S.A. Bernal, Z. Zhao, Z. Shi, N. Belie, Understanding the carbonation of concrete with supplementary cementitious materials: A critical review by RILEM TC 281-CCC, Mater. Struct. 53 (6) (2020) http://dx.doi.org/10.1617/s11527-020-01558-w.
[68] F. Georget, A. Babaahmadi, A. Machner, M. Mrak, S. Dolenec, Q.X. Xiong, J. Shiju, D. Snoeck, P. Suraneni, W. Wilson, Measuring chloride binding in cementitious materials: A review by RILEM TC 298-EBD, Mater. Struct. 58 (10) (2025) 348, http://dx.doi.org/10.1617/s11527-025-02802-x.